



# Adjustable heterointerface-vacancy enhancement effect in $\text{RuO}_2@\text{Co}_3\text{O}_4$ electrocatalysts for efficient overall water splitting

Yong Jiang<sup>a,b,1</sup>, Hao Liu<sup>a,b,1</sup>, Yimin Jiang<sup>a,b</sup>, Yini Mao<sup>a,b</sup>, Wei Shen<sup>a,b</sup>, Ming Li<sup>a,b</sup>, Rongxing He<sup>a,b,\*</sup>

<sup>a</sup> Key Laboratory of Luminescence Analysis and Molecular Sensing (Southwest University), Ministry of Education, PR China

<sup>b</sup> College of Chemistry and Chemical Engineering, Southwest University, Chongqing 400715, PR China

## ARTICLE INFO

### Keywords:

Heterointerface-Vacancy  
Controllable synthesis  
Catalytic activity  
Synergistic effect  
Overall water splitting

## ABSTRACT

Revealing the nature of enhanced catalytic activity by oxygen vacancy and hetero-interface is an important and challenging task. Herein, the high-performance  $\text{RuO}_2@\text{Co}_3\text{O}_4$  electrocatalyst with adjustable heterointerface-vacancy enhancement effect was prepared for the first time. The as-prepared  $\text{RuO}_2@\text{Co}_3\text{O}_4(1:6)$  only respectively requires overpotentials of 152, 218 mV for OER and 90, 33 mV for HER in alkaline and acidic solutions to achieve a current density of  $10 \text{ mA cm}^{-2}$ . Moreover, the assembled electrolytic cell just need a voltages of 1.46, 1.65 V and 1.52, 1.72 V to achieve 10 and  $350 \text{ mA cm}^{-2}$  under the same conditions. The different ratios of Ru and Co can regulate the number of hetero-interfaces between  $\text{RuO}_2$  and  $\text{Co}_3\text{O}_4$  and the concentration of interfacial oxygen vacancies. The systematically experimental and theoretical results unveil that the hetero-interface with strong electron coupling between  $\text{RuO}_2$  and  $\text{Co}_3\text{O}_4$  accelerates the reaction kinetic and improves the stability of the catalyst. The interfacial oxygen vacancy not only directly participates in the reaction of dissociating  $\text{H}_2\text{O}$ , but also adjusts the position of the d-band center of the catalyst and the adsorption strength of key intermediates, thus enhancing the activity of the catalysts.

## 1. Introduction

Water electrolysis is considered to be the most promising approach to generate hydrogen, and the amount of hydrogen produced by this method accounts for 4% of the global total hydrogen production [1–5]. Generally, water electrolysis includes two half-reactions: cathodic hydrogen evolution reaction (HER) and anodic oxygen evolution reaction (OER) [1,6–9]. However, the slow kinetics and high energy consumption of OER seriously hinder the development of water electrolysis. Although many efforts have been made to alleviate the above dilemmas, there are still some problems that have not received enough attention, such as the proton concentration change in water electrolysis is always unavoidable and significantly affects the reaction efficiency, etc. Therefore, the ideal catalyst should be able to adapt to a wide pH range and work stably for a long time [10–13]. Noble metal catalysts usually have good activity, but their poor stability in a wide pH range and their easy oxidation to high valence solubles are still significant drawback. Therefore, it is an urgent need to design efficient and stable alternatives

that can work in a wide pH range.

As a non-metallic oxide with spinel structure,  $\text{Co}_3\text{O}_4$  is widely used in alkaline electrocatalytic water splitting due to its excellent electrochemical stability [14–17]. Unfortunately, the poor electrical conductivity, high working potential and inferior intrinsic activity are still the inherent drawback for  $\text{Co}_3\text{O}_4$  in practical applications [18,19]. Recently, vacancy construction, doping and heterogeneous interfaces have been considered as the most promising strategies to modulate the electronic structure and further enhance the catalytic performance of  $\text{Co}_3\text{O}_4$  [20–23]. For instance, Wang et al. proposed an effective method to regulate electronic structure of  $\text{Co}_3\text{O}_4$  by introducing oxygen vacancy by P-doping, which not only improves the poor conductivity, but also provides more active sites [24]. Lou et al. prepared a series of transition metal doped ultra-thin  $\text{Co}_3\text{O}_4$  nanosheets by chemical etching. These doped catalysts with special structures expose abundant active sites and facilitate charge and mass transport, thus can work stably for 50 h at the current density of  $100 \text{ mA cm}^{-2}$  [25]. Yu et al. constructed a heterogeneous  $\text{RuO}_2/\text{Co}_3\text{O}_4$  by a simple template method, and the formed

\* Corresponding author at: Key Laboratory of Luminescence Analysis and Molecular Sensing (Southwest University), Ministry of Education, PR China.  
E-mail address: [herx@swu.edu.cn](mailto:herx@swu.edu.cn) (R. He).

<sup>1</sup> These authors contributed equally to this work.

heterogeneous interface can promote charge transfer and optimize the adsorption strength of key intermediates [18]. Very recently, Nan et al. prepared the RuO<sub>2</sub>-Co<sub>3</sub>O<sub>4</sub> nanohybrids utilizing Co in ZIF-67 and doped Ru, and considered that the rich oxygen vacancies and large specific surface area caused by synergistic effect are the fundamental reasons for the high catalytic activity [15]. These previous studies manifested that the vacancy and hetero-interface can greatly improve the OER activity of Co<sub>3</sub>O<sub>4</sub>, because they not only adjust the electronic structure and expose more active sites of catalysts, but also optimize the adsorption strength of key intermediates [26,27]. However, there is a key issue that has never been paid much attention, that is, whether oxygen vacancy can directly participate in electrocatalytic reactions? Only by clarifying this problem can we deeply understand the essence of oxygen vacancy enhancing catalyst activity. Another important problem is that most reported methods either cannot prepare catalysts with both vacancies and hetero-interfaces, or they are over-complicated. Can ones develop a new method to simply and controllable prepare catalysts with both oxygen vacancies and hetero-interfaces?

Herein, the RuO<sub>2</sub>@Co<sub>3</sub>O<sub>4</sub> electrocatalyst with adjustable content hetero-interfaces and oxygen vacancies is one-step synthesized by changing the amount of Ru (Note that the one-step process here refers to the one-step synthesis of the precursor, and the preparation of the catalysts requires calcination of the precursor). In this method, Ru<sup>3+</sup> ions and Co<sup>2+</sup> ones are simultaneously added to the solution, then Co<sup>2+</sup> is first reduced to produce Co nanoparticles (NPs) due to its much higher concentration than Ru<sup>3+</sup> (a small amount of Ru may be contained in the Co NPs due to the co-reduction). Subsequently, Ru<sup>3+</sup> and Co<sup>2+</sup> are co-reduced on the surface of the NPs, thereby generating the RuCo precursor with uniformly distributed atoms on the surface of the Co NPs [28]. Finally, the desired RuO<sub>2</sub>@Co<sub>3</sub>O<sub>4</sub> catalyst was obtained by calcination of the precursor in air. This method can obtain a series of catalysts with different amounts of hetero-interfaces and oxygen vacancies on the surface by adjusting the ratio of Ru<sup>3+</sup> and Co<sup>2+</sup>. As expected, the designed RuO<sub>2</sub>@Co<sub>3</sub>O<sub>4</sub>(1:6) (here 1:6 refers to the feed ratio of Ru<sup>3+</sup> and Co<sup>2+</sup>) possesses excellent OER and HER performances in a wide pH range. Moreover, the assembled cell only needs voltage of 1.46 and 1.52 V to achieve 10 mA cm<sup>-2</sup> in alkaline and acidic solutions. The experimental and DFT results verify that the strong electronic coupling between RuO<sub>2</sub> and Co<sub>3</sub>O<sub>4</sub> promotes charge redistribution at the interface, which is beneficial to improve the activity and stability of the catalyst. More importantly, interfacial oxygen vacancy not only regulates the position of the d-band center, promotes the adsorption of key intermediates, but also acts as an active site for efficient H<sub>2</sub>O dissociation, thus enhancing the performance of the catalyst.

## 2. Experimental section

### 2.1. Chemicals and materials

Sodium borohydride (NaBH<sub>4</sub>), ruthenium(III) chloride (RuCl<sub>3</sub>), cobalt chloride (CoCl<sub>2</sub>·6 H<sub>2</sub>O) and potassium hydroxide (KOH) were purchased from Shanghai Aladdin Biochemical Technology Co. Ltd. Pt/C (20 wt% Pt on Vulcan XC-72R), ruthenium (IV) oxide (RuO<sub>2</sub>) and Nafion (5 wt%) were purchased from Sigma Aldrich chemical reagent. Sulfuric acid was purchased from Chongqing Chuandong Chemical Co. Ltd. Carbon paper was purchased from Shanghai Hesen Electric Co. Ltd. All reagents were directly used without further purification.

### 2.2. Synthesis of RuO<sub>2</sub>@Co<sub>3</sub>O<sub>4</sub> NPs

Firstly, the RuCo precursor was prepared by a facile room temperature reduction method. In detail, 30 mg of RuCl<sub>3</sub> and 180 mg of CoCl<sub>2</sub>·6H<sub>2</sub>O are dissolved in deionized water and sonicated for 0.5 h to obtained a uniform mixture solution. Then, the prepared NaBH<sub>4</sub> solution was dropped slowly into the mixture solution at a stirring speed of 500 rpm/min. Finally, stop dropping NaBH<sub>4</sub> solution when the black solid

precipitates and the solution becomes clear. Filter the transparent solution and washed the black solid with deionized water, and then dry it in the oven at 60 °C for 6 h. RuO<sub>2</sub>@Co<sub>3</sub>O<sub>4</sub>(1:6) was obtained by annealing the black solid in a tubular furnace at 600 °C for 3 h. By changing the added amount of RuCl<sub>3</sub> and keeping the amount of CoCl<sub>2</sub>·6 H<sub>2</sub>O, RuO<sub>2</sub>@Co<sub>3</sub>O<sub>4</sub>(1:9), RuO<sub>2</sub>@Co<sub>3</sub>O<sub>4</sub>(1:4) and RuO<sub>2</sub>@Co<sub>3</sub>O<sub>4</sub>(1:3) can be obtained after the same treatment.

### 2.3. Preparation of working electrode

5.0 mg catalyst, 0.28 mL deionized water, 0.20 mL absolute ethanol and 0.02 mL Nafion (5 wt%) were sonicated for 30 min, then 0.05 mL dispersion was evenly coated on 1 × 1 cm<sup>2</sup> carbon paper, it can be used for electrochemical test after drying.

### 2.4. Material characterization

The surface morphologies and element composition of the catalysts were characterized by scanning electron microscopy (SEM; Hitachi Flex SEM 1000) and transmission electron microscopy (TEM; FEI Talos F200S). Powder X-ray diffraction (XRD; Bruker D2 PHASER) was used to obtain the crystallographic informations of the catalysts. Chemical state of elements in catalysts were performed by X-ray photoelectron spectroscopy (XPS; Thermo Scientific k-alpha). The contents of Ru and Co in the catalysts were detected by inductively coupled plasma spectrometry (ICP-OES; Agilent 5110).

### 2.5. XAFS measurements

The X-ray absorption fine structure spectrum (Fe K-edge) was gathered at 1W1B station in Beijing Synchrotron Radiation Facility (BSRF). The storage rings of BSRF were operated at 2.5 GeV with an average current of 250 mA. Using a Si(111) double-crystal monochromator, the data acquisition was performed in the transmission/fluorescence mode through an ionization chamber. All spectra were measured under ambient condition.

### 2.6. XAFS analysis and results

Use the ATHENA module implemented in the IFEFFIT software package to process the obtained EXAFS data according to the standard program. The k<sup>3</sup>-weighted EXAFS spectra were achieved by subtracting the post-edge background from the total absorption and normalizing the edge-jump step. Then, using a hanning windows (dk = 1.0 Å<sup>-1</sup>), the k<sup>3</sup>-weighted χ(k) data of Fe K-edge were transformed to real (R) space by Fourier transform to separate the EXAFS contributions of different coordination shells. To obtain the quantitative structural parameters around central atoms, the least-squares curve parameter fitting was performed using the ARTEMIS module of the IFEFFIT software package [29–31].

### 2.7. Electrochemical measurements

All electrochemical tests were completed on CHE 760E electrochemical workstation using a standard three electrode test system. Wherein, the working electrode (working area is 1 × 1 cm<sup>2</sup>) is loaded catalyst carbon paper, the counter electrode is a graphite rod, and the reference electrode uses Hg/HgO and Ag/AgCl in alkaline and acidic environment, respectively. Commercial catalysts Pt/C and RuO<sub>2</sub> with the same loading amounts were used as reference catalysts for HER and OER, respectively. All measured potentials are converted to standard hydrogen electrode potential according to the following formula:

$$E_{RHE} = E_{Hg/HgO} + 0.0591 \times pH + E_{Hg/HgO}^* (\text{In alkaline media})$$

$$E_{RHE} = E_{Ag/AgCl} + 0.0591 \times pH + E_{Ag/AgCl}^* (\text{In acid media}).$$

Owing to the resistance between interface of catalysts and electrolytes, the iR compensation was performed with the values of 95%. The scanning rate of all electrochemical polarization curves is 5 mV/s, and the Tafel slope was calculate by Tafel equation:

$$\eta = b \times \log j + a$$

where  $\eta$  is the overpotential,  $b$  is the Tafel slope,  $j$  is the current density, and  $a$  is the constant).

## 2.8. Theoretical calculations

Density functional theory (DFT) is calculated by Vienna ab initio simulation package (VASP) with exchange correlation functional. The interaction between core electrons and ions was described by a projector truncated wave (PAW) with a truncation energy of 400 eV [32–37]. The k-point of Brillouin zone is set to  $2 \times 2 \times 1$  for structural optimization. The vacuum layer in the z-axis direction was set at 15 Å to prevent periodic boundary action. In addition, all models are relaxed in calculation, and the convergence standard of energy is  $10^{-6}$  eV, and the convergence standard of force is  $0.02 \text{ eV}\text{\AA}^{-1}$ . RuO<sub>2</sub> (101) and Co<sub>3</sub>O<sub>4</sub> (311) were selected for construction RuO<sub>2</sub>@Co<sub>3</sub>O<sub>4</sub> heterostructure.

The Gibbs free energy of four elementary reactions of OER in acidic environment was calculated as follows:

$$\Delta G_1 = G_{\text{OH}^*} + G_{\text{H}^+ + e^-} - G_{\text{H}_2\text{O}(l)} - G_*$$

$$\Delta G_2 = G_{\text{O}^*} + G_{\text{H}^+ + e^-} - G_{\text{OH}^*}$$

$$\Delta G_3 = G_{\text{OOH}^*} + G_{\text{H}^+ + e^-} - G_{\text{H}_2\text{O}(l)} - G_{\text{O}^*}$$

$$\Delta G_4 = G_{\text{O}^*} + G_{\text{O}_2(g)} + G_{\text{H}^+ + e^-} - G_{\text{OOH}^*}$$

The Gibbs adsorption free energy of HER reaction H\* refers to the following formula:

$$\Delta G_{\text{H}^*} = \Delta E_{\text{H}^*} + \Delta \text{ZPE} - T\Delta S$$

where  $\Delta E_{\text{H}^*}$  was the hydrogen chemisorption energy,  $\Delta \text{ZPE}$  and  $\Delta S$  were the zero-point energy difference and the entropy difference between the adsorbed and the gas phase, respectively.

## 3. Results and discussion

### 3.1. Preparation and characterization of catalysts

RuO<sub>2</sub>@Co<sub>3</sub>O<sub>4</sub> was obtained by calcining the precursor RuCo NPs, and the detailed preparation process was shown in Fig. S1. The RuCl<sub>3</sub>·H<sub>2</sub>O and CoCl<sub>2</sub>·6H<sub>2</sub>O were dissolved in deionized water, and sodium borohydride solution was dropped slowly into the mixed solution until the formation of black powder (RuCo NPs), then the black powder was calcined at 600 °C in air for 3 h, the final sample was recorded as RuO<sub>2</sub>@Co<sub>3</sub>O<sub>4</sub>. When the ratio of Ru and Co is 1:6, the catalyst RuO<sub>2</sub>@Co<sub>3</sub>O<sub>4</sub>(1:6) with the best electrocatalytic performance is obtained. If the ratio of Ru and Co is changed to 1:3, there is no Co<sub>3</sub>O<sub>4</sub> on the obtained catalyst surface due to the coverage of excessive Ru. When the proportion becomes 1:9 by decreasing the amount of Ru, no RuO<sub>2</sub> is found on the prepared catalyst surface (see XPS analysis for details). The catalysts formed by the latter two Ru:Co ratios (1:3 and 1:9) contain less hetero-interfaces and oxygen vacancies, proving that the present synthesis method can controllably adjust the concentration of hetero-interfaces and oxygen vacancies on the catalyst surface.

As shown in Fig. S2, the phase structure and crystallographic information of RuO<sub>2</sub>@Co<sub>3</sub>O<sub>4</sub>(1:6) were performed by X-ray powder diffraction (XRD), and the pure RuO<sub>2</sub> and Co<sub>3</sub>O<sub>4</sub> were set as reference samples. The peaks at 28.0°, 35.0° and 54.5° correspond to (110), (101) and (211) crystal planes of RuO<sub>2</sub> (PDF #88–0323), respectively, and the peaks located at 36.8°, 59.3° and 65.2° can match well with (311), (511) and

(440) planes of Co<sub>3</sub>O<sub>4</sub> (PDF #74–2120), which indicates a large number of RuO<sub>2</sub> and Co<sub>3</sub>O<sub>4</sub> coexist on the surface of the RuO<sub>2</sub>@Co<sub>3</sub>O<sub>4</sub>(1:6) catalyst. The diffraction peaks of RuO<sub>2</sub>@Co<sub>3</sub>O<sub>4</sub>(1:6) are slightly shifted compared with the pure RuO<sub>2</sub> and Co<sub>3</sub>O<sub>4</sub>, which confirms that the synthesized catalyst has a heterostructure formed by the chemical coupling between RuO<sub>2</sub> and Co<sub>3</sub>O<sub>4</sub>, rather than their mixture. In addition, the XRD images of the prepared samples with different Ru and Co ratios were shown in Fig. S3. The diffraction peak intensity of RuO<sub>2</sub> gradually strengthens, and that of Co<sub>3</sub>O<sub>4</sub> progressively decreases with ratio of Ru and Co changing from 1:9–1:3. In the XRD pattern of RuO<sub>2</sub>@Co<sub>3</sub>O<sub>4</sub>(1:3), only the characteristic diffraction peak of RuO<sub>2</sub> is displayed, which indicates that in this case, the excessive Ru atoms completely cover the surface of catalyst precursor. Contrarily, the characteristic peaks of Co<sub>3</sub>O<sub>4</sub> are dominant in the XRD spectrum of RuO<sub>2</sub>@Co<sub>3</sub>O<sub>4</sub>(1:9), which demonstrates that a large amount of Co atoms are distributed on the surface of the catalyst precursor. The above results verify that catalysts with different contents of RuO<sub>2</sub> and Co<sub>3</sub>O<sub>4</sub> on the surface can be prepared by changing the ratio of Ru and Co, thereby realizing controllable synthesis of hetero-interfaces with different concentrations. To prove this simple one-step method can controllably synthesize the RuO<sub>2</sub>@Co<sub>3</sub>O<sub>4</sub>(1:x) catalysts with such special structure, a conventional two-step method is adopted for synthesizing the catalysts. In this method, the first step is to add NaBH<sub>4</sub> to the solution containing only Co<sup>2+</sup> to prepare pure Co NPs. The second step is to put the generated Co NPs into a solution with different content of Ru<sup>3+</sup>, in which Ru<sup>3+</sup> will be reduced to Ru atoms and uniformly adhere to the surface of Co NPs, and finally to obtain the precursor RuCo-2 (the precursor here is named as RuCo-2 to distinguish it from the one-step precursor RuCo). After calcination in air, the catalyst named RuO<sub>2</sub>@Co<sub>3</sub>O<sub>4</sub>(1:x)–2 is obtained. As shown in Figs. S3 and S4, the XPS spectra of RuO<sub>2</sub>@Co<sub>3</sub>O<sub>4</sub>(1:x)–2 synthesized by the two-step method are almost the same as those of the corresponding RuO<sub>2</sub>@Co<sub>3</sub>O<sub>4</sub>(1:x) catalysts prepared by the one-step method. Further, the electrochemical performance (Fig. S5) of the two kinds of catalysts is almost the same (the slight difference should be from different synthesis methods). All of these prove that the RuO<sub>2</sub>@Co<sub>3</sub>O<sub>4</sub>(1:x) catalysts with this special hetero-interfaces can be synthesized in a controllable way by the one-step method.

Scanning electron microscopy (SEM) is used to reveal the morphology of precursor RuCo(1:6) (Fig. 1a) and catalyst RuO<sub>2</sub>@Co<sub>3</sub>O<sub>4</sub>(1:6) NPs (Fig. 1b), the results show that the size of RuO<sub>2</sub>@Co<sub>3</sub>O<sub>4</sub>(1:6) NPs is obviously larger than that of RuCo(1:6), confirming that the metal oxides was successfully prepared, this is consistent with the XRD results (Figs. S2 and S6). Moreover, no obvious agglomeration of RuO<sub>2</sub>@Co<sub>3</sub>O<sub>4</sub>(1:6) was observed in the high resolution transmission electron microscopy (HRTEM) image, indicating that the catalyst has an outstanding physical stability (Fig. 1c). The magnified TEM image (Fig. 1d) clearly displays the heterogeneous interface between RuO<sub>2</sub> and Co<sub>3</sub>O<sub>4</sub> in RuO<sub>2</sub>@Co<sub>3</sub>O<sub>4</sub>(1:6), and the lattice spacing of RuO<sub>2</sub> and Co<sub>3</sub>O<sub>4</sub> are 0.254 and 0.248 nm, respectively. It is worth noting that the interfacial oxygen vacancies can also be clearly observed at the amplified heterogeneous interface (Fig. 1e). The TEM-EDX elemental mapping further proves the existence of O, Co and Ru, which are evenly distributed over the whole catalyst (Fig. 1f–i).

X-ray photoelectron spectroscopy (XPS) was adopted to analyze the surface components and chemical states of the obtained catalysts. As shown in Fig. S7, the peaks located at binding energies of 529.10 and 530.05 eV can be assigned to the lattice oxygen species and the M-O bonds [20–23]. The intensity of M-O peak in RuO<sub>2</sub>@Co<sub>3</sub>O<sub>4</sub>(1:6) is much larger than those in RuO<sub>2</sub> and Co<sub>3</sub>O<sub>4</sub>, which may be due to the formation of -Ru-O-Co- bonds at the hetero-interface of the catalyst. Importantly, the characteristic peak of oxygen vacancy (near 531.5 eV) in RuO<sub>2</sub>@Co<sub>3</sub>O<sub>4</sub>(1:6) is also observed. Compared with the precursor RuCo, the RuO<sub>2</sub>@Co<sub>3</sub>O<sub>4</sub>(1:6) sample shows a strong symmetrical signal (g=2.003) in the electron paramagnetic resonance (EPR) spectrum, which demonstrates the existence of a large number of oxygen vacancies in the



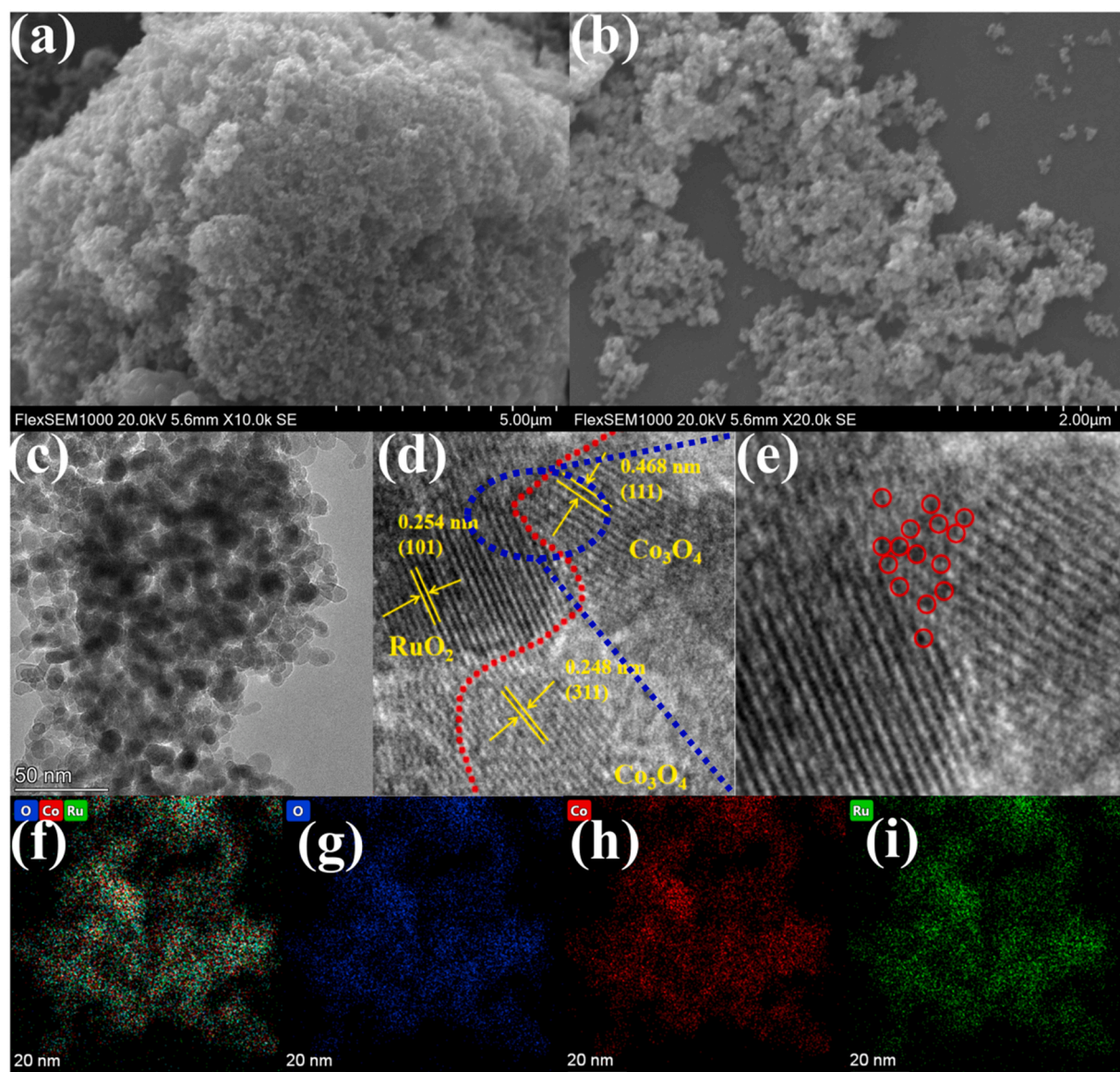


**Fig. 1.** Scanning electron microscope of (a) precursor RuCo and (b) RuO<sub>2</sub>@Co<sub>3</sub>O<sub>4</sub>(1:6). (c) HRTEM image of RuO<sub>2</sub>@Co<sub>3</sub>O<sub>4</sub>(1:6) heterojunction. (d) Magnified TEM image of RuO<sub>2</sub>@Co<sub>3</sub>O<sub>4</sub>(1:6) hetero-interface. (e) Magnified TEM image of RuO<sub>2</sub>@Co<sub>3</sub>O<sub>4</sub>(1:6) interfacial oxygen vacancies. (f-i) TEM-EDX elemental mapping distribution diagram.

as-prepared RuO<sub>2</sub>@Co<sub>3</sub>O<sub>4</sub>(1:6) catalyst (Fig. S8). The O1s spectra of RuO<sub>2</sub>@Co<sub>3</sub>O<sub>4</sub>(1:9), RuO<sub>2</sub>@Co<sub>3</sub>O<sub>4</sub>(1:6), RuO<sub>2</sub>@Co<sub>3</sub>O<sub>4</sub>(1:4) and RuO<sub>2</sub>@Co<sub>3</sub>O<sub>4</sub>(1:3) were shown in Fig. S9 and Table S1. It can be seen that the concentration of oxygen vacancy raises rapidly with the decrease of Ru:Co ratio, and reaches the maximum when Ru:Co is 1:6, then decreases with the continuous reduction of Ru:Co ratio (such as 1:9). It means that the number of hetero-interfaces on the catalyst surface is the largest only when the Ru:Co ratio is 1:6 (see XRD analysis), thus the amount of vacancies induced by the hetero-interfaces is also the largest. If the ratio is higher than 1:6 (such as 1:3), Ru on the catalyst surface is much more than Co; on the contrary, Co almost completely covers the catalyst surface. In these two cases, the number of vacancies induced by hetero-interfaces will be significantly reduced. The above discussion verifies that by changing the ratio of Ru:Co, the one-step method developed in this work can not only regulate the number of Ru and Co thus the concentration of RuO<sub>2</sub>@Co<sub>3</sub>O<sub>4</sub> hetero-interfaces, but also adjust the content of oxygen vacancies at the interface, thus realizing the controllable synthesis of high-performance electrocatalysts with both oxygen vacancies and hetero-interfaces.

As shown in Fig. 2a, the Ru 3d peaks of RuO<sub>2</sub>@Co<sub>3</sub>O<sub>4</sub>(1:6) are negatively shifted by 0.3 eV compared with those of the contrast samples (RuO<sub>2</sub> and RuO<sub>2</sub> + Co<sub>3</sub>O<sub>4</sub>), and the peaks of RuO<sub>2</sub> and the physical mixture (RuO<sub>2</sub> + Co<sub>3</sub>O<sub>4</sub>) are almost identical. These findings confirm that there is a strong electronic interaction between RuO<sub>2</sub> and Co<sub>3</sub>O<sub>4</sub> in RuO<sub>2</sub>@Co<sub>3</sub>O<sub>4</sub>(1:6). The peaks located at 280.95, 282.82 and 281.62 eV are assigned to RuO<sub>2</sub>, RuO<sub>3</sub> and Sat. peak [38,39], respectively. In Fig. 2b, the three peaks at binding energies of 779.08, 780.38 and 787.58 eV are assigned to Co<sup>3+</sup>, Co<sup>2+</sup> and Sat. peak, respectively [40–42]. Notably, the binding energies for Co 2p band of RuO<sub>2</sub>@Co<sub>3</sub>O<sub>4</sub>(1:6) are positively shifted by 0.8 eV compared with other samples, suggesting the existence of electron transfer from Co<sub>3</sub>O<sub>4</sub> to RuO<sub>2</sub> due to the strong electronic coupling at the hetero-interfaces.

X-ray absorption near edge structure (XANES) and the extended X-ray absorption fine structure (EXAFS) spectra were further performed to determine the fine structure of RuO<sub>2</sub>@Co<sub>3</sub>O<sub>4</sub>(1:6) and the chemical state of Ru and Co. For comparison, the XANES and EXAFS spectra of Co<sub>3</sub>O<sub>4</sub>, RuO<sub>2</sub>, Co foil and Ru foil were also measured. As shown in Figs. 3a and 3b, the absorption threshold positions of Co<sub>3</sub>O<sub>4</sub> and RuO<sub>2</sub> in

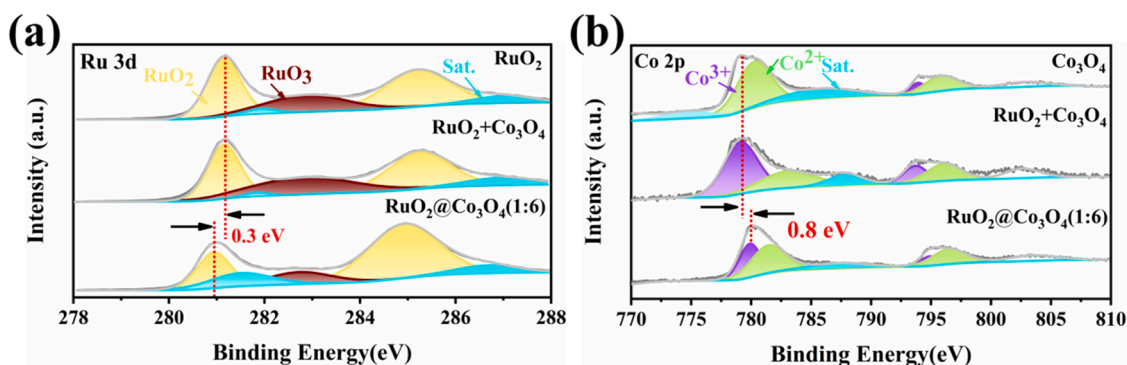


Fig. 2. XPS spectra of Ru 3d (a) and Co 2p (b) for RuO<sub>2</sub>, mixture of RuO<sub>2</sub>+Co<sub>3</sub>O<sub>4</sub>, and RuO<sub>2</sub>@Co<sub>3</sub>O<sub>4</sub>(1:6).

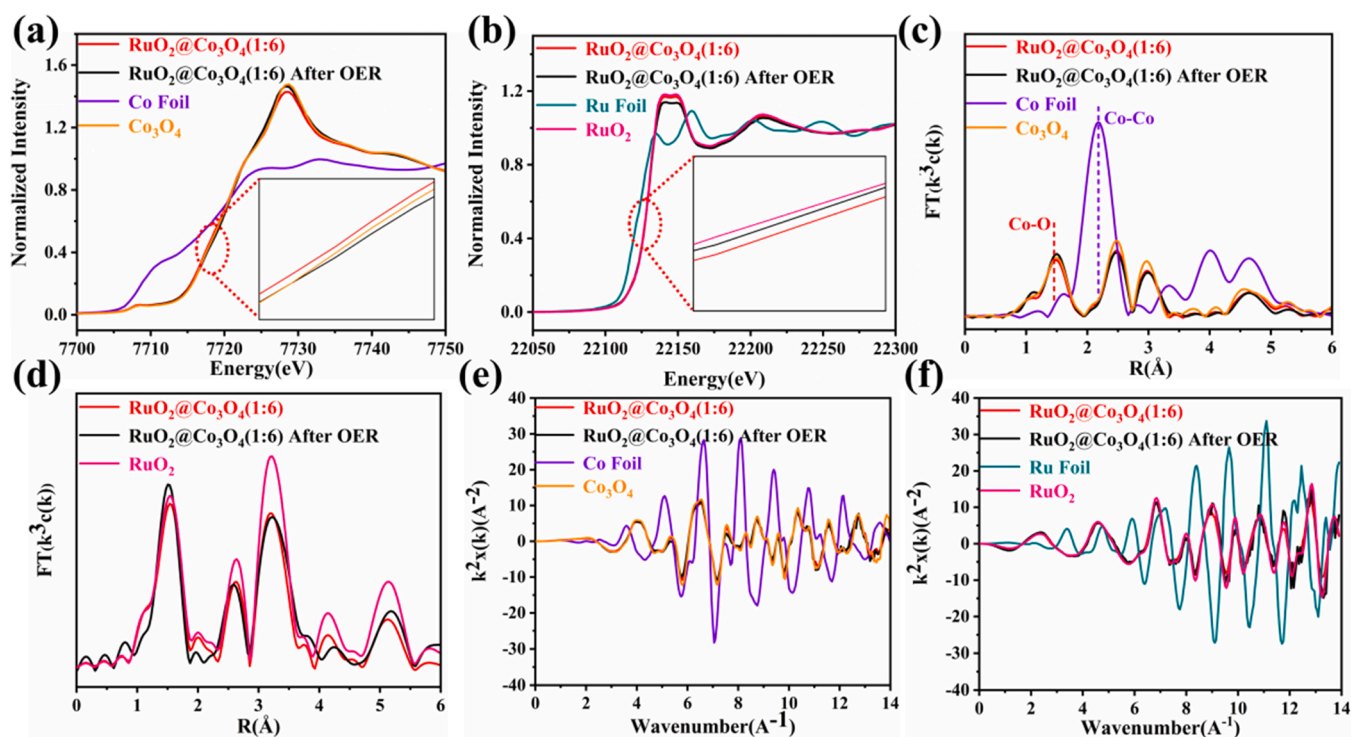


Fig. 3. (a-b) Co and Ru K-edge XANES spectra for RuO<sub>2</sub>@Co<sub>3</sub>O<sub>4</sub>(1:6), RuO<sub>2</sub>@Co<sub>3</sub>O<sub>4</sub>(1:6) after OER, Co foil, Co<sub>3</sub>O<sub>4</sub>, Ru foil and RuO<sub>2</sub>, the inset image is amplified rising edge of the XANES spectra. (c-d) R space and corresponding inverse FT-EXAFS results of RuO<sub>2</sub>@Co<sub>3</sub>O<sub>4</sub>(1:6), RuO<sub>2</sub>@Co<sub>3</sub>O<sub>4</sub>(1:6) after OER, Co foil, Co<sub>3</sub>O<sub>4</sub> and RuO<sub>2</sub>. (e-f) Co and Ru K-edge EXAFS oscillations spectra for RuO<sub>2</sub>@Co<sub>3</sub>O<sub>4</sub>(1:6), RuO<sub>2</sub>@Co<sub>3</sub>O<sub>4</sub>(1:6) after OER, Co foil, Co<sub>3</sub>O<sub>4</sub>, Ru foil and RuO<sub>2</sub>.

RuO<sub>2</sub>@Co<sub>3</sub>O<sub>4</sub>(1:6) have no obvious change compared with that of the pure Co<sub>3</sub>O<sub>4</sub> and RuO<sub>2</sub>, indicating that the oxidation states of Co and Ru in RuO<sub>2</sub>@Co<sub>3</sub>O<sub>4</sub>(1:6) are basically unchanged after the formation of heterojunction, which is also verified by their EXAFS spectra (Figs. 3c and 3d), in which the intensities of the Co–O and Ru–O shells of RuO<sub>2</sub>@Co<sub>3</sub>O<sub>4</sub>(1:6) are almost the same as those of the pure Co<sub>3</sub>O<sub>4</sub> and RuO<sub>2</sub>. However, the absorption threshold position of Co<sub>3</sub>O<sub>4</sub> in RuO<sub>2</sub>@Co<sub>3</sub>O<sub>4</sub>(1:6) after OER tests shifts slightly to higher energy (inset of Fig. 3a) compared to that of Co<sub>3</sub>O<sub>4</sub> in RuO<sub>2</sub>@Co<sub>3</sub>O<sub>4</sub>(1:6) before OER tests, implying that the oxidation state of Co increases slightly. Meanwhile, it is found that the absorption position of RuO<sub>2</sub> in RuO<sub>2</sub>@Co<sub>3</sub>O<sub>4</sub>(1:6) hardly changes before and after OER tests (inset of Fig. 3b). These results demonstrate that Co should be the active site of OER [43–45]. As shown in Fig. 3c and d, the EXAFS spectra show that the distances of Co–O and Ru–O are respectively 1.47 and 1.51 Å for RuO<sub>2</sub>@Co<sub>3</sub>O<sub>4</sub>(1:6) before OER tests, while those for the pure Co<sub>3</sub>O<sub>4</sub> and RuO<sub>2</sub> is 1.51 and 1.53 Å, respectively (Table S2). The remarkable increase of M–O (M represents Co and Ru) bond length confirms the

existence of strong interface coupling between RuO<sub>2</sub> and Co<sub>3</sub>O<sub>4</sub> in RuO<sub>2</sub>@Co<sub>3</sub>O<sub>4</sub>(1:6). The fitting M–O bond lengths for various samples and coordination number of metal centers are respectively displayed in Fig. S10 and Table S3. Obviously, the coordination number of Co center decreases from 5.4 of pure Co<sub>3</sub>O<sub>4</sub> to 4.6 of RuO<sub>2</sub>@Co<sub>3</sub>O<sub>4</sub>(1:6). This may be because the formation of heterogeneous interfaces induces the generation of oxygen vacancies at the interface, thus reducing the coordination number of Co center, which is also consistent with the results of XPS and EPR. Moreover, the coordination number of Co in RuO<sub>2</sub>@Co<sub>3</sub>O<sub>4</sub>(1:6) increases from 4.6 before OER to 5.0 after OER, indicating the formation of more high-valence Co ions. The high-valence Co ions not only act as the active site for OER [14], but also contribute to the stability of the catalyst [16], which is also confirmed by the strong peak of M–O bond observed before and after OER shown in Figs. 3e and f [18]. In addition, the M–O coordination mode of Co and Ru was observed both in RuO<sub>2</sub>@Co<sub>3</sub>O<sub>4</sub>(1:6) before and after the test (Figs. 3e and f), indicating that the catalyst still maintains the metal oxide structure, which again confirms that the catalyst has good stability.



### 3.2. Electrochemical performance

The electrochemical hydrogen evolution activities of the prepared catalysts were evaluated in 1.0 M KOH and 0.5 M H<sub>2</sub>SO<sub>4</sub> solutions via standard three electrode system. As shown in Fig. S11, the overpotential of RuO<sub>2</sub>@Co<sub>3</sub>O<sub>4</sub>(1:6) is much lower than those of RuO<sub>2</sub>, Co<sub>3</sub>O<sub>4</sub> and the physical mixture in both alkaline and acidic environments, which verifies that the strong electronic coupling at hetero-interface of RuO<sub>2</sub>@Co<sub>3</sub>O<sub>4</sub>(1:6) can effectively improve the HER activity of the catalyst. Figs. 4a and 4b display the HER performance of all samples with different ratios of Ru and Co in alkaline and acidic solutions. Although the overpotential of RuO<sub>2</sub>@Co<sub>3</sub>O<sub>4</sub>(1:4) (45 and 28 mV to reach 10 mA cm<sup>-2</sup>) is smaller than that of RuO<sub>2</sub>@Co<sub>3</sub>O<sub>4</sub>(1:6) (90 and 33 mV) in both alkaline and acidic media, the OER activity of RuO<sub>2</sub>@Co<sub>3</sub>O<sub>4</sub>(1:6) is the best among them (see Fig. 5). Considering the performance of overall water splitting, RuO<sub>2</sub>@Co<sub>3</sub>O<sub>4</sub>(1:6) is mainly introduced here. Obviously, the overpotential of RuO<sub>2</sub>@Co<sub>3</sub>O<sub>4</sub>(1:6) in acidic medium is close to that of the commercial Pt/C (33 mV vs 16 mV), showing the promising potentials to replace the precious metal electrocatalysts, which is also supported by the data shown in Table S4, where the delivered HER performance of RuO<sub>2</sub>@Co<sub>3</sub>O<sub>4</sub>(1:6) is superior to those of most reported Co oxides. Tafel slopes of RuO<sub>2</sub>@Co<sub>3</sub>O<sub>4</sub>(1:6) are 103 and 95 mV dec<sup>-1</sup> in alkaline and acidic media, which is much higher than those of the commercial Pt/C (33 and 31 mV dec<sup>-1</sup>) following the Tafel mechanism, indicating the reaction kinetics of RuO<sub>2</sub>@Co<sub>3</sub>O<sub>4</sub>(1:6) follows the Volmer-Heyrovsky mechanism (Fig. 4c and d) [46–48]. Further, RuO<sub>2</sub>@Co<sub>3</sub>O<sub>4</sub>(1:6) also show very low overpotential (140 and 175 mV) at high current densities of 100 and 300 mA cm<sup>-2</sup> (Fig. 4e and f) and can work stably in alkaline environment more than 500 h (Fig. S12), which means that the catalyst has great application prospects. Importantly, it can be found that if the ratio of Ru and Co is too large or too small, the HER activity of the catalyst will be reduced. This is because the Ru content on the catalyst surface is low when the ratio is too small, while Ru may agglomerate on the surface when the ratio is too large, which indicates that Ru should be the active site of HER.

Impressively, RuO<sub>2</sub>@Co<sub>3</sub>O<sub>4</sub>(1:6) exhibits the best OER performance with an ultra-low overpotential of 152 and 219 mV to achieve a current density of 10 mA cm<sup>-2</sup> in alkaline and acidic media, which is about 100 mV less than that of the state-of-the-art RuO<sub>2</sub> (253 and 329 mV) and much lower than that of the pure RuO<sub>2</sub> and Co<sub>3</sub>O<sub>4</sub> under the same conditions (Figs. 5a, b and S13). This result proves once again that the oxygen vacancies and electronic coupling between RuO<sub>2</sub> and Co<sub>3</sub>O<sub>4</sub> at the hetero-interfaces can greatly boost the OER activity of the catalysts. As shown Fig. 5c and d, RuO<sub>2</sub>@Co<sub>3</sub>O<sub>4</sub>(1:6) has the lowest Tafel slope of 68 and 73 mV dec<sup>-1</sup> in alkaline and acidic solutions, which is significantly smaller than those of all the other samples studied including commercial RuO<sub>2</sub>. The lower Tafel slope suggests the faster kinetics of the water oxidation process on the surfaces of RuO<sub>2</sub>@Co<sub>3</sub>O<sub>4</sub>(1:6). It is worth mentioning that RuO<sub>2</sub>@Co<sub>3</sub>O<sub>4</sub>(1:6) just need ultra-low overpotential of 198 and 260 mV to achieve high current density of 100 and 300 mA cm<sup>-2</sup> (Fig. 5e and f), which is one of the best OER catalysts reported in alkaline solution to date (Table S5). To illuminate the intrinsic activity of catalysts, the turnover frequency (TOF) of RuO<sub>2</sub>@Co<sub>3</sub>O<sub>4</sub>(1:6), the benchmarks Pt/C and RuO<sub>2</sub> was tested (see Fig. S16 and Table S6). The TOF value of RuO<sub>2</sub>@Co<sub>3</sub>O<sub>4</sub>(1:6) for HER is slightly lower than that of commercial Pt/C at an overpotential of 50 mV, while the TOF for OER at 300 mV is about 72 times higher than that of the benchmark RuO<sub>2</sub> in alkaline environment, demonstrating that RuO<sub>2</sub>@Co<sub>3</sub>O<sub>4</sub>(1:6) has excellent intrinsic activity. The C<sub>dl</sub> values of RuO<sub>2</sub>@Co<sub>3</sub>O<sub>4</sub>(1:6), Pt/C and RuO<sub>2</sub> shown in Figs. S17 and S18 are consistent with the results of LSV and TOF. Moreover, the as-expected smallest electrochemical impedance resistance (EIS) demonstrates the favored charge-transfer kinetics of RuO<sub>2</sub>@Co<sub>3</sub>O<sub>4</sub>(1:6), verifying the strong electronic coupling at the hetero-interfaces could accelerate electron transfer (Fig. S19).

Besides the activity, the stability of the electrocatalysts is very important for their practical application. Fig. S20 shows the SEM images of RuO<sub>2</sub>@Co<sub>3</sub>O<sub>4</sub>(1:6) after long-time HER and OER stability tests. It can be seen that the morphology of the RuO<sub>2</sub>@Co<sub>3</sub>O<sub>4</sub>(1:6) NPs remains basically unchanged except for slight agglomeration. The contents of Ru

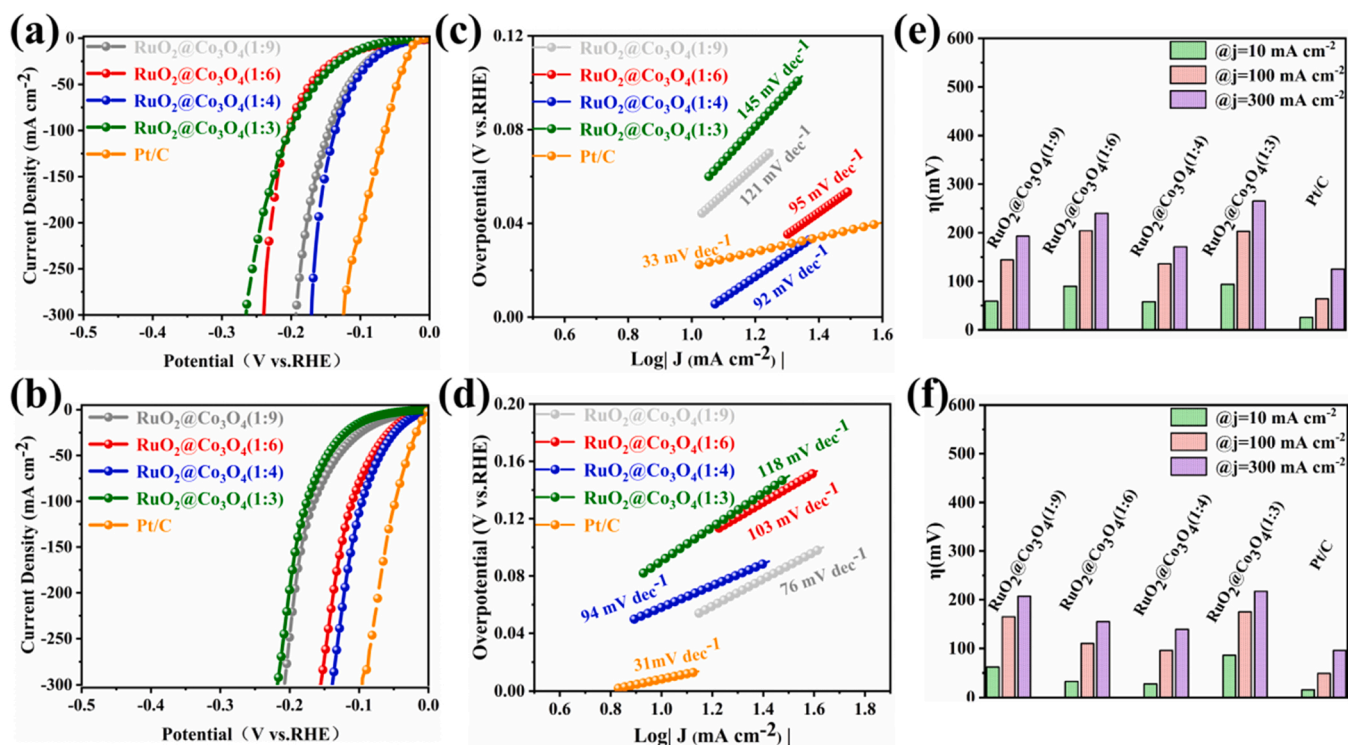
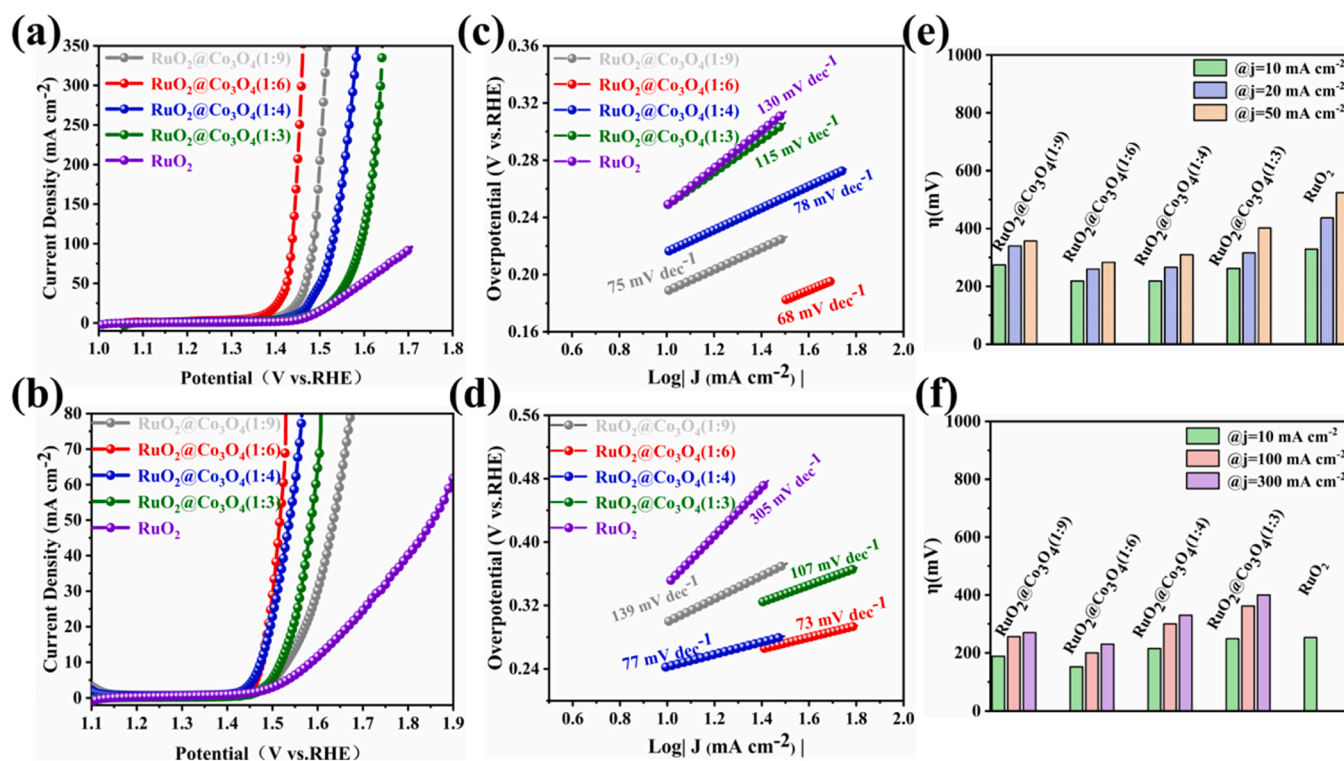


Fig. 4. LSV polarization curves of HER in (a) alkaline and (b) acidic environments. Tafel curves in (c) alkaline and (d) acidic environments. Histogram of overpotential comparison of HER at the current density of 10, 100 and 300 mA cm<sup>-2</sup> in (e) alkaline and (f) acidic environments.



**Fig. 5.** LSV polarization curves of OER in (a) alkaline and (b) acidic solutions. Tafel curves in (c) alkaline and (d) acidic solutions. The overpotential of OER for contrast samples in (e) alkaline (10, 100 and 300 mA cm<sup>-2</sup>) and (f) acidic environments (10, 20 and 50 mA cm<sup>-2</sup>).

and Co dissolved in the electrolyte after the long-term stability test were measured by the ICP-OES spectrum and the results are listed in Table S7. Obviously, the amounts of Ru and Co leached after HER and OER tests in alkaline solution are small, indicating that the RuO<sub>2</sub>@Co<sub>3</sub>O<sub>4</sub>(1:6) NPs are stable even after the long-term stability tests. However, one can find that the dissolved amount of Ru is much larger than that of Co in the OER process, which suggests that Co rather than Ru is the active site of OER. The XPS spectra of RuO<sub>2</sub>@Co<sub>3</sub>O<sub>4</sub>(1:6) after HER and OER stability tests shown in Fig. S21 indicate that the intensity of the oxygen vacancy characteristic peak at the binding energy of 531.5 eV is decreased, which may be due to the surface reconstruction of the catalyst [49]. In particular, CoOOH, Co(OH)<sub>2</sub> [50–52] and soluble Ru(OH)<sub>x</sub> (285.5 eV) were observed in XPS spectra after OER test, which is clear evidence of surface reconstruction.

Encouraged by the excellent HER and OER activity of RuO<sub>2</sub>@Co<sub>3</sub>O<sub>4</sub>(1:6), the performance of overall water-splitting was measured by using RuO<sub>2</sub>@Co<sub>3</sub>O<sub>4</sub>(1:6) as both the anode and cathode. As shown in Fig. 6a, the assembled cell only needs voltages of 1.46 and 1.68 V to achieve current densities of 10 and 350 mA cm<sup>-2</sup> in alkaline environment (it requires a cell voltage of 1.52 V @ 10 mA cm<sup>-2</sup> in acidic medium, see Fig. 6b), which is better than that of Pt/C||RuO<sub>2</sub> electrode and most previously reported advanced catalysts (Table S8). In addition, the stability of the RuO<sub>2</sub>@Co<sub>3</sub>O<sub>4</sub>(1:6)||RuO<sub>2</sub>@Co<sub>3</sub>O<sub>4</sub>(1:6) cell was also tested, and the i-t curve clearly shows that the assembled cell can operate stably for nearly 350 h in 1.0 M KOH solution (Fig. 6c and d), indicating the outstanding durability of RuO<sub>2</sub>@Co<sub>3</sub>O<sub>4</sub>(1:6) in practical overall water splitting.

### 3.3. The origin of enhanced electrocatalytic performance

Density functional theory (DFT) calculations were carried out to illuminate how the atomic level interface engineering regulates the catalytic performance (that is, why RuO<sub>2</sub>@Co<sub>3</sub>O<sub>4</sub>(1:6) possesses enhanced HER and OER activities). Since the oxygen vacancies at the interfaces can be located on RuO<sub>2</sub> or Co<sub>3</sub>O<sub>4</sub>, two calculated models,

RuO<sub>2</sub>@Co<sub>3</sub>O<sub>4</sub>-1 and RuO<sub>2</sub>@Co<sub>3</sub>O<sub>4</sub>-2, are constructed (see Figs. S22 and S23), in which Vo-RuO<sub>2</sub>@Co<sub>3</sub>O<sub>4</sub>-1 represents an oxygen vacancy Vo is sited on RuO<sub>2</sub>, and RuO<sub>2</sub>@Vo-Co<sub>3</sub>O<sub>4</sub>-2 refers to Vo is on Co<sub>3</sub>O<sub>4</sub>. Both the models are based on the experimental results and conform to the real structure of the RuO<sub>2</sub>@Co<sub>3</sub>O<sub>4</sub>(1:6) catalyst. The difference is that the ratio of RuO<sub>2</sub> and Co<sub>3</sub>O<sub>4</sub> in the former is 1:1 and that in the latter is 0.5:1 (if the same model is used, the size of the model needs to be doubled to build oxygen vacancy on RuO<sub>2</sub> or Co<sub>3</sub>O<sub>4</sub>, which requires expensive calculation cost). As shown in Table S9, the dissociation energies of H<sub>2</sub>O on pure RuO<sub>2</sub> (0.73 eV) and pure Co<sub>3</sub>O<sub>4</sub> (0.85 eV) is higher than those on RuO<sub>2</sub>@Co<sub>3</sub>O<sub>4</sub>-1 (0.52 eV) and RuO<sub>2</sub>@Co<sub>3</sub>O<sub>4</sub>-2 (0.61 eV), indicates that the formation of hetero-interfaces contributes to the decomposition of H<sub>2</sub>O. Further, the dissociation energies of H<sub>2</sub>O on a<sub>Ru</sub>-Vo-RuO<sub>2</sub>@Co<sub>3</sub>O<sub>4</sub>-1 (a<sub>Ru</sub> indicates that the active site is located on RuO<sub>2</sub>) and a<sub>Vo</sub>-Vo-RuO<sub>2</sub>@Co<sub>3</sub>O<sub>4</sub>-1 (a<sub>Vo</sub> means Vo is the active site) are respectively 0.43 and 0.49 eV, which are lower than that of RuO<sub>2</sub>@Co<sub>3</sub>O<sub>4</sub>-1 (0.52 eV), indicating that the oxygen vacancy is also conducive to H<sub>2</sub>O dissociation. Interestingly, among all the constructed models, the water decomposition energy on a<sub>Vo</sub>-RuO<sub>2</sub>@Vo-Co<sub>3</sub>O<sub>4</sub>-2 is the lowest with only 0.21 eV (they are 0.48 and 0.44 eV on a<sub>Co</sub>-RuO<sub>2</sub>@Vo-Co<sub>3</sub>O<sub>4</sub>-2 and a<sub>Ru</sub>-RuO<sub>2</sub>@Vo-Co<sub>3</sub>O<sub>4</sub>-2). These theoretical findings strongly prove that the hetero-interfaces and oxygen vacancies greatly promote the dissociation of water molecules in the as-prepared catalyst. Specially, the oxygen vacancies near the interface on Co<sub>3</sub>O<sub>4</sub> are most likely to directly participate in the electrocatalytic process as the active sites for H<sub>2</sub>O dissociation, which is the first time to clearly explain the role of oxygen vacancy in the electrocatalytic decomposition of water. Further, the calculated Gibbs free energy of hydrogen adsorption on RuO<sub>2</sub>@Co<sub>3</sub>O<sub>4</sub>-1 (-0.24 eV) is much higher than those of pure RuO<sub>2</sub> (-0.35 eV) and Co<sub>3</sub>O<sub>4</sub> (-0.46 eV), illuminating that the strong electron coupling between RuO<sub>2</sub> and Co<sub>3</sub>O<sub>4</sub> is also beneficial to enhance the HER activity (Fig. S24a). To further evaluate the effect of oxygen vacancy on the HER performance, the free energies of hydrogen adsorption on the three models with oxygen vacancies were calculated and the results are shown in Fig. 7a. Obviously, a<sub>Ru</sub>-RuO<sub>2</sub>@Vo-Co<sub>3</sub>O<sub>4</sub>-2 has the adsorption energy

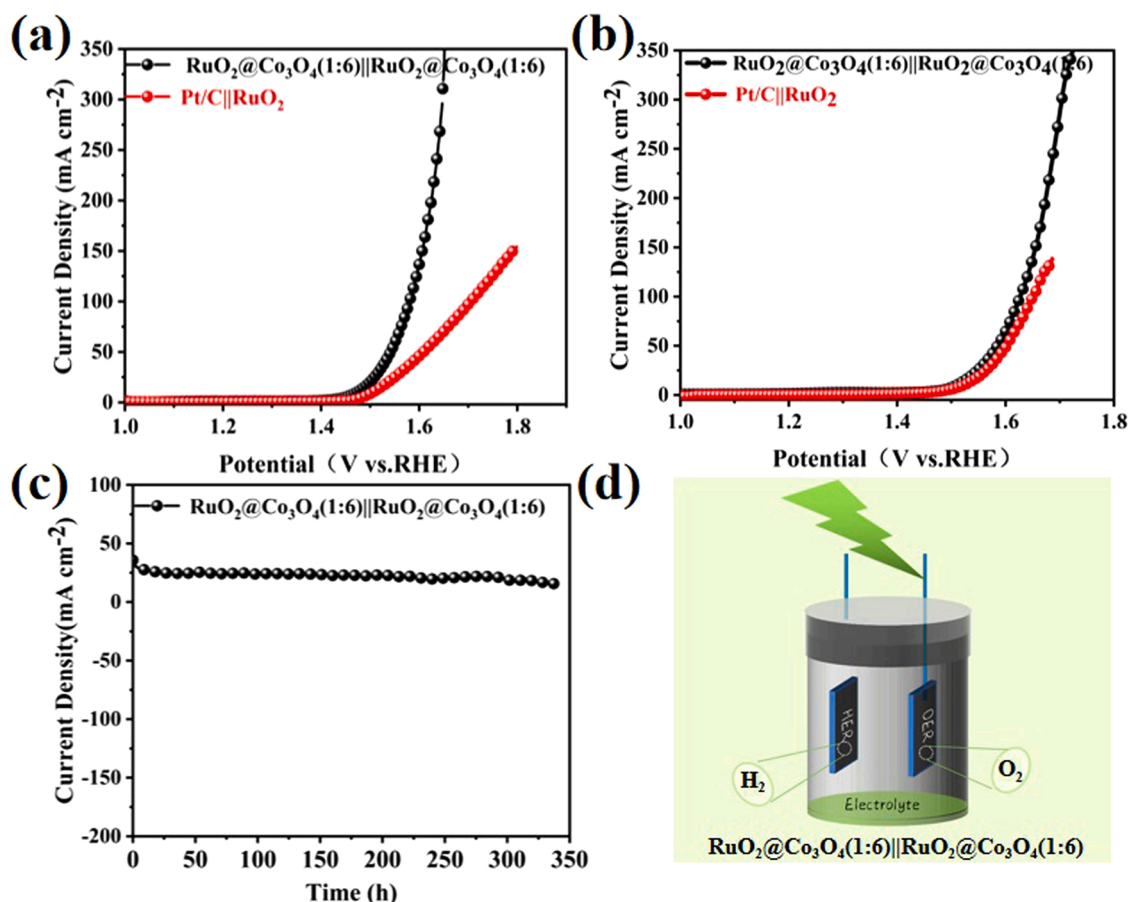


**Fig. 6.** (a) LSV polarization curves of water electrolysis in alkaline and (b) acidic environments. (c) i-t stability test curve of water electrolysis in alkaline environment. (d) Schematic diagram of water electrolysis.

closest to zero ( - 0.09 eV), which not only verifies that the oxygen vacancy on Co<sub>3</sub>O<sub>4</sub> rather than RuO<sub>2</sub> is the most favorable to improve the HER activity of the catalyst, but also indicates that Ru is the active sites of HER.

To further explore the origin of excellent OER activity, the adsorption free energies of the four oxygen-based intermediates in the OER mechanism on all models were calculated, as displayed in Figs. 7b, 7c and S24. The results show that for all the models, the energy barrier of the elementary reaction  $O^* \rightarrow HOO^*$  is higher than those of the other three elementary steps ( $H_2O^* \rightarrow HO^*$ ,  $HO^* \rightarrow O^*$ ,  $HOO^* \rightarrow O_2$ ), illustrating that this step is the rate-determining step (RDS) of OER. The results shown in Figs. S24b and S24c suggest that the electron coupling between RuO<sub>2</sub> and Co<sub>3</sub>O<sub>4</sub> is important for improving OER activity due to the lowest RDS energy barrier on RuO<sub>2</sub>@Co<sub>3</sub>O<sub>4</sub>-1. In order to investigate the effect of the position of oxygen vacancy (on RuO<sub>2</sub> or Co<sub>3</sub>O<sub>4</sub>) on the OER performance, the Gibbs free energies of four models with oxygen vacancy for OER process were calculated. As shown in Fig. 7b and S24d, a<sub>Co</sub>-RuO<sub>2</sub>@Vo-Co<sub>3</sub>O<sub>4</sub>-2 has the best OER activity compared with the other three contrast samples because of its lowest overpotential of only 0.16 V. Combining the analysis results of HER and OER, it can be found that the HER and OER performance of the as-prepared catalyst are the best when the oxygen vacancies near the interface are located on Co<sub>3</sub>O<sub>4</sub>. Fig. 7c and S25 further demonstrate that oxygen vacancies do contribute to the improvement of OER activity of the catalyst. It is generally known that the performance of electrocatalysts is closely related to their activity of decomposing H<sub>2</sub>O. Therefore, from the perspective of dynamics, we calculated the transition states of water molecule decomposition on the models a<sub>V</sub>-RuO<sub>2</sub>@Vo-Co<sub>3</sub>O<sub>4</sub>-2, a<sub>Co</sub>-RuO<sub>2</sub>@Vo-Co<sub>3</sub>O<sub>4</sub>-2 and a<sub>Ru</sub>-RuO<sub>2</sub>@Vo-Co<sub>3</sub>O<sub>4</sub>-2. As displayed in Fig. 7d, the activation energy of

water decomposition on model a<sub>V</sub>-RuO<sub>2</sub>@Vo-Co<sub>3</sub>O<sub>4</sub>-2 is the lowest with only 0.16 eV, which confirms that the oxygen vacancies on Co<sub>3</sub>O<sub>4</sub> are indeed the active sites of water decomposition and directly participate in the reaction [53]. This conclusion is completely consistent with the thermodynamic results obtained in the previous paragraph.

To clarify the intrinsic nature of hetero-interfaces and oxygen vacancies enhancing catalyst activity, work function, density of states (DOS) and charge density distribution were also carried out. The work function represents the minimum energy required in a semiconductor to move electron at the Fermi level into a vacuum, that is, the smaller the work function, the easier the electron transfer. As shown in Fig. S26, among the four calculated models, their work function values are RuO<sub>2</sub> (6.08 eV) > RuO<sub>2</sub>@Co<sub>3</sub>O<sub>4</sub>-1 (5.94 eV) > Vo-RuO<sub>2</sub>@Co<sub>3</sub>O<sub>4</sub>-1 (5.75 eV) > RuO<sub>2</sub>@Vo-Co<sub>3</sub>O<sub>4</sub>-2 (5.65 eV). This result verifies that the formed RuO<sub>2</sub>@Co<sub>3</sub>O<sub>4</sub> hetero-interfaces and oxygen vacancies can significantly accelerate the electron transfer (see the EIS result), thus enhancing the activity of the catalyst. In fact, the strong coupling between RuO<sub>2</sub> between Co<sub>3</sub>O<sub>4</sub> inevitably leads to the redistribution of charge density at the interface (see Fig. S27), which will generate enhanced dipole polarization at the RuO<sub>2</sub>@Co<sub>3</sub>O<sub>4</sub> hetero-interface, thereby accelerating the electron transfer and improving the catalytic activity [54,55]. This is consistent with the results of work function and the XPS analysis. Fig. 7e gives the DOS of d-band of RuO<sub>2</sub>, RuO<sub>2</sub>@Co<sub>3</sub>O<sub>4</sub>-1, Vo-RuO<sub>2</sub>@Co<sub>3</sub>O<sub>4</sub>-1 and RuO<sub>2</sub>@Vo-Co<sub>3</sub>O<sub>4</sub>-2 models, and the position of their d-band center are - 1.93, - 1.64, - 1.53 and - 1.72 eV, respectively. It is well known that the shift of the d-band center away from the Fermi energy level leads to the decreased adsorption energy between intermediates and catalyst surfaces [56]. This indicates that among them, the adsorption strength on RuO<sub>2</sub> is the smallest and that on RuO<sub>2</sub>@Vo-Co<sub>3</sub>O<sub>4</sub>-1 is the



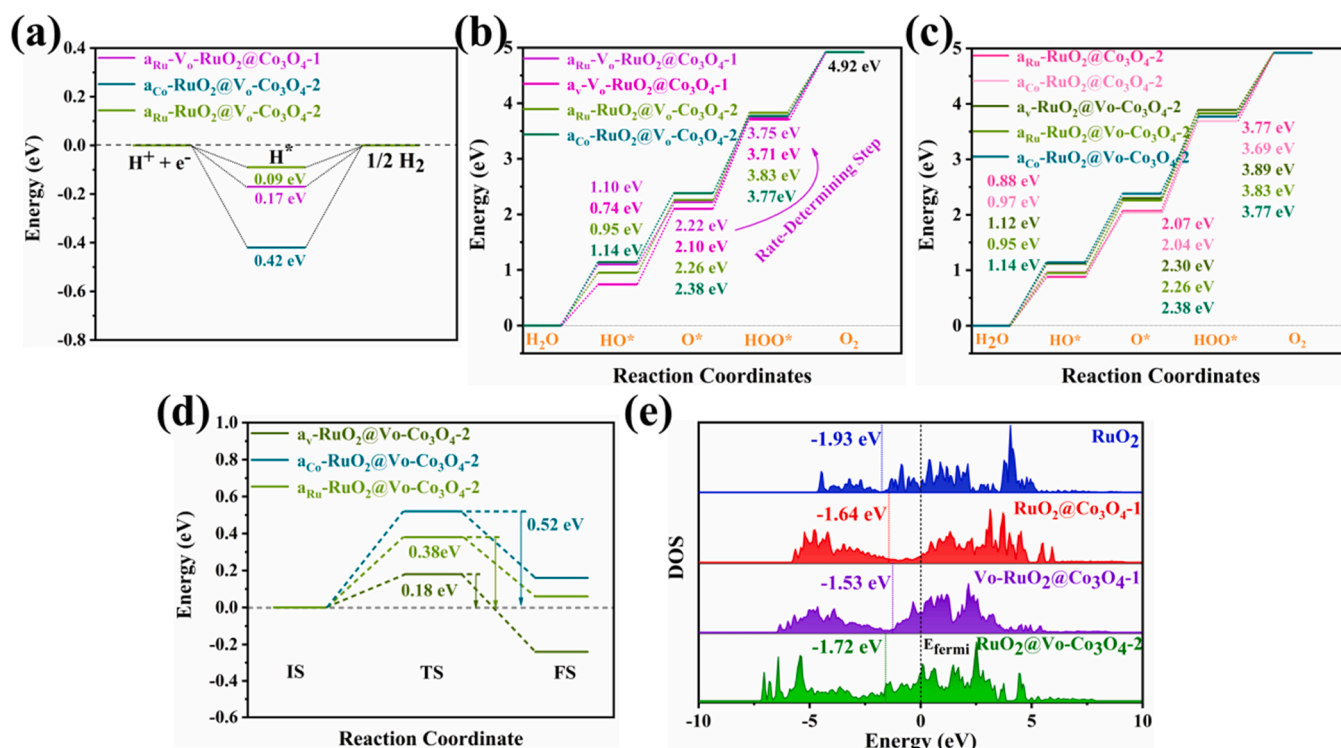


Fig. 7. (a) H-Gibbs adsorption free energy of a<sub>Ru</sub>-V<sub>O</sub>-RuO<sub>2</sub>@Co<sub>3</sub>O<sub>4</sub>-1, a<sub>Co</sub>-RuO<sub>2</sub>@V<sub>O</sub>-Co<sub>3</sub>O<sub>4</sub>-2 and a<sub>Ru</sub>-RuO<sub>2</sub>@V<sub>O</sub>-Co<sub>3</sub>O<sub>4</sub>-2. (b) OER energy barrier at different sites on Vo-RuO<sub>2</sub>@Co<sub>3</sub>O<sub>4</sub>-1 and RuO<sub>2</sub>@Vo-Co<sub>3</sub>O<sub>4</sub>-2 models. (c) The effect of vacancy on OER at different sites in RuO<sub>2</sub>@Co<sub>3</sub>O<sub>4</sub>-2 model. (d) Dissociation energy of H<sub>2</sub>O at vacancy, Ru and Co sites in RuO<sub>2</sub>@Vo-Co<sub>3</sub>O<sub>4</sub>-2, respectively. (e) d-band center level of RuO<sub>2</sub>, RuO<sub>2</sub>@Co<sub>3</sub>O<sub>4</sub>-1, Vo-RuO<sub>2</sub>@Co<sub>3</sub>O<sub>4</sub>-1 and RuO<sub>2</sub>@Vo-Co<sub>3</sub>O<sub>4</sub>-2.

largest. According to the Sabatier principle [57,58], too strong or too weak adsorption strength is not conducive to electrocatalytic reaction. These findings verify that the catalyst with oxygen vacancies distributed on Co<sub>3</sub>O<sub>4</sub>, RuO<sub>2</sub>@Vo-Co<sub>3</sub>O<sub>4</sub>-2, has the best catalytic performance due to its optimal adsorption strength. Moreover, the partial DOS (PDOS) of elements in Co<sub>3</sub>O<sub>4</sub>, RuO<sub>2</sub>, RuO<sub>2</sub>@Co<sub>3</sub>O<sub>4</sub>-1, Vo-RuO<sub>2</sub>@Co<sub>3</sub>O<sub>4</sub>-1 and RuO<sub>2</sub>@Vo-Co<sub>3</sub>O<sub>4</sub>-2 shown in Fig. S28 reveals that the hetero-interfaces and oxygen vacancies in the catalyst greatly increase the density of states near the Fermi level (especially Co and Ru), which is conducive to improving the electronic conductivity and electron transfer ability, thus greatly enhancing the electrocatalytic performance of the catalyst.

#### 4. Conclusions

In summary, the controllable synthesis of highly active and stable electrocatalyst with hetero-interfaces and oxygen vacancies, RuO<sub>2</sub>@Co<sub>3</sub>O<sub>4</sub>, was realized for the first time using a facile one-step method. It is revealed that the Ru:Co ratio can adjust the concentration of hetero-interfaces and oxygen vacancies on the catalyst surface. Experimental and DFT results confirmed that the hetero-interfaces and oxygen vacancies induced by strong chemical coupling between RuO<sub>2</sub> and Co<sub>3</sub>O<sub>4</sub> lead to the redistribution of charge density and the shift of d-band center, which increase the electronic conductivity and optimize the adsorption strength of intermediates, thus greatly improving the catalyst performance. The XANES and EXAFS spectra confirmed that Ru and Co are respectively the active sites of HER and OER. Interestingly, a series of control experiments and theoretical calculations strongly proved that oxygen vacancy on Co<sub>3</sub>O<sub>4</sub> of the catalyst are most beneficial to the improvement of catalytic activity, and it directly participates in the electrocatalytic reaction as active site of water splitting. This synergistic effect of hetero-interface and oxygen vacancy in the as-prepared RuO<sub>2</sub>@Co<sub>3</sub>O<sub>4</sub> catalyst contributes to the excellent HER and OER activities and achieves outstanding overall water splitting performance. This work provides a method for controllable synthesis of high-performance

electrocatalysts with hetero-interface and vacancy, and a new idea for exploring the essential role of oxygen vacancy in electrocatalytic water splitting.

#### CRediT authorship contribution statement

Yong Jiang and Hao Liu contributed to experiments, calculations, data collation and manuscript writing, Yimin Jiang, Yini Mao and Wei Shen contributed to discussion and calculation guidance, Ming Li and Rongxing He contributed to the proposal of innovation, funding acquisition and manuscript modification.

#### Declaration of Competing Interest

The authors declare that they have no known competing financial interests or personal relationships that could have appeared to influence the work reported in this paper.

#### Data Availability

Data will be made available on request.

#### Acknowledgements

We acknowledge the financial supports from National Natural Science Foundation of China (91741105, 22006120), Program for Innovation Team Building at Institutions of Higher Education in Chongqing (CXTDX201601011) and the General Project of Chongqing Frontier and Applied Basic Research Program (cstc2020jcyj-msxmX0536).

#### Appendix A. Supporting information

Supplementary data associated with this article can be found in the online version at doi:10.1016/j.apcatb.2022.122294.

## References

- [1] Z.-C. Chen, L. Guo, L. Pan, T.-Q. Yan, Z.-X. He, Y. Li, C.-X. Shi, Z.-F. Huang, X.-W. Zhang, J.-J. Zou, Advances in oxygen evolution electrocatalysts for proton exchange membrane water electrolyzers, *Adv. Energy Mater.* (2022), 2103670.
- [2] A. Kumar, P. Daw, D. Milstein, Homogeneous catalysis for sustainable energy: hydrogen and methanol economies, fuels from biomass, and related topics, *Chem. Rev.* 122 (2022) 385–441.
- [3] X.-H. Xie, L. Du, L.-T. Yan, S. Park, Y. Qiu, J. Sokolowski, W. Wang, Y.-Y. Shao, Oxygen evolution reaction in alkaline environment: material challenges and solutions, *Adv. Funct. Mater.* 32 (2022), 2110036.
- [4] Z. Yan, J.-L. Hitt, J.-A. Turner, T.-E. Mallouk, Renewable electricity storage using electrolysis, *Proc. Natl. Acad. Sci.* 117 (2020) 12558–12563.
- [5] W.-J. Jiang, T. Tang, Y. Zhang, J.-S. Hu, Synergistic modulation of non-precious-metal electrocatalysts for advanced water splitting, *Acc. Chem. Res.* 53 (2020) 1111–1123.
- [6] T.-Q. Guo, L.-D. Li, Z.-C. Wang, Recent development and future perspectives of amorphous transition metal-based electrocatalysts for oxygen evolution reaction, *Adv. Energy Mater.* 12 (2022), 2200827.
- [7] R. Li, H. Wang, F. Hu, K.-C. Chan, X. Liu, Z. Lu, J. Wang, Z. Li, L. Zeng, Y. Li, X. Wu, Y. Xiong, Y. IrW, Nanochannel support enabling ultrastable electrocatalytic oxygen evolution at 2 A cm<sup>-2</sup> in acidic media, *Nat. Commun.* 12 (2021) 3540.
- [8] B.-B. Zhang, T.-Y. Lu, Y.-P. Ren, L.-Z. Huang, H. Pang, Q. Zhao, S. Tian, J. Yang, L. Xu, Y.-W. Tang, X.-L. Tian, Encapsulation of Co/Co<sub>3</sub>O<sub>4</sub> hetero-nanoparticles within the inner tips of N-doped carbon nanotubes: engineering Mott-Schottky nanoreactors for efficient bifunctional oxygen electrocatalysis toward flexible zinc-air batteries, *Chem. Eng. J.* 448 (2022), 137709.
- [9] H. Ding, H. Liu, W. Chu, C. Wu, Y. Xie, Structural transformation of heterogeneous materials for electrocatalytic oxygen evolution reaction, *Chem. Rev.* 121 (2021) 13174–13212.
- [10] T. Zhu, S. Liu, B. Huang, Q. Shao, M. Wang, F. Li, X. Tan, Y. Pi, S.-C. Weng, B. Huang, Z. Hu, J. Wu, Y. Qian, X. Huang, High-performance diluted nickel nanoclusters decorating ruthenium nanowires for pH-universal overall water splitting, *Energy Environ. Sci.* 14 (2021) 3194–3202.
- [11] T. Zheng, C. Shang, Z. He, X. Wang, C. Cao, H. Li, R. Si, B. Pan, S. Zhou, J. Zeng, Intercalated iridium diselenide electrocatalysts for efficient pH-universal water splitting, *Angew. Chem. Int. Ed. Engl.* 58 (2019) 14764–14769.
- [12] W. Zhang, X. Jiang, Z. Dong, J. Wang, N. Zhang, J. Liu, G.R. Xu, L. Wang, Porous Pd/NiFeOx nanosheets enhance the pH-universal overall water splitting, *Adv. Funct. Mater.* 31 (2021), 2107181.
- [13] L. Zhuang, F. Xu, K. Wang, J. Li, C. Liang, W. Zhou, Z. Xu, Z. Shao, Z. Zhu, Porous structure engineering of iridium oxide nanoclusters on atomic scale for efficient pH-universal overall water splitting, *Small* 17 (2021), e2100121.
- [14] Z. Liu, L.-L. Zeng, J.-Y. Yu, L.-J. Yang, J. Zhang, X.-L. Zhang, F. Han, L.-L. Zhao, X. Li, H. Liu, W.-J. Zhou, Charge redistribution of Ru nanoclusters on Co<sub>3</sub>O<sub>4</sub> porous nanowire via the oxygen regulation for enhanced hydrogen evolution reaction, *Nano Energy* 85 (2021), 105940.
- [15] Y. Zhang, S.-T. Zhang, J. Ma, A.-J. Huang, M.-W. Yuan, Y.-F. Li, G.-B. Sun, C. Chen, C.-Y. Nan, Oxygen vacancy-rich RuO<sub>2</sub>-Co<sub>3</sub>O<sub>4</sub> nanohybrids as improved electrocatalysts for Li-O<sub>2</sub> batteries, *ACS Appl. Mater. Interfaces* 13 (2021) 39239–39247.
- [16] Z.-H. Xiao, Y.-C. Huang, C.-L. Dong, C. Xie, Z.-J. Liu, S.-Q. Du, W. Chen, D.-F. Yan, L. Tao, Z.-W. Shu, G.-H. Zhang, H.-G. Duan, Y.-Y. Wang, Y.-Q. Zou, R. Chen, S.-Y. Wang, Operando identification of the dynamic behavior of oxygen vacancy-rich Co<sub>3</sub>O<sub>4</sub> for oxygen evolution reaction, *J. Am. Chem. Soc.* 142 (2020) 12087–12095.
- [17] R.-R. Zhang, Y.-C. Zhang, L. Pan, G.-Q. Shen, N. Mahmood, Y.-H. Ma, Y. Shi, W.-Y. Jia, L. Wang, X.-W. Zhang, W. Xu, J.-J. Zou, Engineering cobalt defects in cobalt oxide for highly efficient electrocatalytic oxygen evolution, *ACS Catal.* 8 (2018) 3803–3811.
- [18] X.-J. Zhuang, Y.-T. Zhou, Z.-Q. Jiang, X.-Z. Yao, X.-Y. Yu, Synergetic electronic modulation and nanostructure engineering of heterostructured RuO<sub>2</sub>/Co<sub>3</sub>O<sub>4</sub> as advanced bifunctional electrocatalyst for zinc-air batteries, *J. Mater. Chem. A* 9 (2021) 26669.
- [19] Y.-Y. Liang, Y.-G. Li, H.-L. Wang, J.-G. Zhou, J. Wang, T. Regier, H.-J. Dai, Co<sub>3</sub>O<sub>4</sub> nanocrystals on graphene as a synergistic catalyst for oxygen reduction reaction, *Nat. Mater.* 10 (2011) 780–786.
- [20] L. Xiao, D. Wang, M. Li, B.-H. Deng, J.-P. Liu, Hybrid architecture design enhances the areal capacity and cycling life of low-overpotential nanoarray oxygen electrode for lithium–oxygen batteries, *J. Energy Chem.* 46 (2020) 248–255.
- [21] M. Tahir, L. Pan, R. Zhang, Y.-C. Wang, G. Shen, I. Aslam, M.A. Qadeer, N. Mahmood, W. Xu, L. Wang, X. Zhang, J.-J. Zou, High-valence-state NiO/Co<sub>3</sub>O<sub>4</sub> nanoparticles on nitrogen-doped carbon for oxygen evolution at low overpotential, *ACS Energy Lett.* 2 (2017) 2177–2182.
- [22] H. Yuan, S. Wang, Z. Ma, M. Kundu, B. Tang, J. Li, X. Wang, Oxygen vacancies engineered self-supported B doped Co<sub>3</sub>O<sub>4</sub> nanowires as an efficient multifunctional catalyst for electrochemical water splitting and hydrolysis of sodium borohydride, *Chem. Eng. J.* 404 (2021), 126474.
- [23] X. Du, Y. Ding, X. Zhang, Selectively Se-doped Co<sub>3</sub>O<sub>4</sub>/CeO<sub>2</sub> nanoparticle-dotted nanoneedle arrays for high-efficiency overall water splitting, *Appl. Surf. Sci.* 562 (2021), 150277.
- [24] Z. Xiao, Y. Wang, Y.-C. Huang, Z. Wei, C.-L. Dong, J. Ma, S. Shen, Y. Li, S. Wang, Filling the oxygen vacancies in Co<sub>3</sub>O<sub>4</sub> with phosphorus: an ultra-efficient electrocatalyst for overall water splitting, *Energy Environ. Sci.* 10 (2017) 2563–2569.
- [25] S.-L. Zhang, B.-Y. Guan, X.-F. Lu, S. Xi, Y. Du, X.-W.D. Lou, Metal atom-doped Co<sub>3</sub>O<sub>4</sub> hierarchical nanoplates for electrocatalytic oxygen evolution, *Adv. Mater.* 32 (2020), e2002235.
- [26] Q. Wang, H. Xu, X.-Y. Qian, G.-Y. He, H.-Q. Chen, Oxygen and sulfur dual vacancies engineering on 3D Co<sub>3</sub>O<sub>4</sub>/CoS<sub>2</sub> heterostructure to improve overall water splitting activity, *Green. Chem.* (2022), <https://doi.org/10.1039/D2GC03315A>.
- [27] N. Yao, R. Meng, F. Wu, Z.-Y. Fan, G.-Z. Cheng, W. Luo, Oxygen-Vacancy-Induced CeO<sub>2</sub>/Co<sub>3</sub>N heterostructures toward enhanced pH-universal hydrogen evolution reactions, *Appl. Catal. B: Environ.* 277 (2020), 119282.
- [28] Y. Jiang, Y.-N. Mao, Y.-M. Jiang, H. Liu, W. Shen, M. Li, R.-X. He, Atomic equidistribution enhanced RuIr electrocatalysts for overall water splitting in the whole pH range, *Chem. Eng. J.* 450 (2022), 137909.
- [29] B. Ravel, M. Newville, ATHENA, ARTEMIS, HEPHAESTUS: data analysis for X-ray absorption spectroscopy using IFEFFIT, *J. Synchrotron Radiat.* 12 (2005) 537–541.
- [30] D.C. Koningsberger, R. Prins, in: D.C. Koningsberger, R. Prins (Eds.), *X-ray Absorption: Principles, Applications, Techniques of EXAFS, SEXAFS, and XANES*, Vol. 92, Wiley, 1988.
- [31] J.J. Rehr, R.C. Albers, Theoretical approaches to X-ray absorption fine structure, *Rev. Mod. Phys.* 72 (2000) 621–654.
- [32] G. Kresse, J. Furthmüller, Efficiency of ab-initio total energy calculations for metals and semiconductors using a plane-wave basis set, *Computational. Mater. Sci.* 6 (1996) 15–50.
- [33] G. Kresse, J. Furthmüller, Efficient iterative schemes for ab initio total-energy calculations using a plane-wave basis set, *Phys. Rev. B* 54 (1996) 11169–11186.
- [34] J.P. Perdew, K. Burke, M. Ernzerhof, Generalized gradient approximation made simple, *Phys. Rev. Lett.* 77 (1996) 3865–3868.
- [35] J.P. Perdew, M. Ernzerhof, K. Burke, Rationale for mixing exact exchange with density functional approximations, *J. Chem. Phys.* 105 (1996) 9982–9985.
- [36] G. Kresse, D. Joubert, From ultrasoft pseudopotentials to the projector augmented-wave method, *Phys. Rev. B* 59 (1999) 1758–1775.
- [37] G. Henkelman, A. Arnaldsson, H. Jónsson, A fast and robust algorithm for Bader decomposition of charge density, *Computational. Mater. Sci.* 36 (2006) 354–360.
- [38] Y. Fan, X. Zhang, Y. Zhang, X. Xie, J. Ding, J. Cai, B. Li, H. Lv, L. Liu, M. Zhu, X. Zheng, Q. Cai, Y. Liu, S. Lu, Decoration of Ru/RuO<sub>2</sub> hybrid nanoparticles on MoO<sub>2</sub> plane as bifunctional electrocatalyst for overall water splitting, *J. Colloid Interface Sci.* 604 (2021) 508–516.
- [39] T.-J. Qiu, J.-Q. Cheng, Z.-B. Liang, H. Tabassum, J.-M. Shi, Y.-Q. Tang, W.-H. Guo, L.-R. Zheng, S. Gao, S.-Z. Xu, R.-Q. Zou, Unveiling the nanoalloying modulation on hydrogen evolution activity of ruthenium-based electrocatalysts encapsulated by B/N co-doped graphitic nanotubes, *Appl. Catal. B: Environ.* 316 (2022), 121626.
- [40] T. Zhang, F. Song, Y. Wang, J. Yuan, L. Niu, K. Fang A.-J. Wang, Bifunctional WS<sub>2</sub>/Co<sub>3</sub>S<sub>4</sub> core-shell nanowire arrays for efficient water splitting, *Electro Acta* 404 (2022), 139648.
- [41] P.K.L. Tran, D.T. Tran, D. Malhotra, S. Prabhakaran, D.H. Kim, N.H. Kim, J.H. Lee, Highly efficient freshwater and seawater electrolysis enabled by atomic Rh-Modulated Co-CoO lateral heterostructures, *Small* 17 (2021), e2103826.
- [42] J. Yao, M. Zhang, X. Ma, L. Xu, F. Gao, J. Xiao, H. Gao, Interfacial electronic modulation of CoP-CoO p-p type heterojunction for enhancing oxygen evolution reaction, *J. Colloid Interface Sci.* 607 (2022) 1343–1352.
- [43] X.-L. Fan, C. Liu, M.-Y. Wu, B.-X. Gao, L.-Y. Zheng, Y.-H. Zhang, H.-B. Zhang, Q.-S. Gao, X.-M. Cao, Y. Tang, Synergistic effect of dual active sites over Ru/α-MoC for accelerating alkaline hydrogen evolution reaction, *Appl. Catal. B: Environ.* 318 (2022), 121867.
- [44] Y.-T. Zhang, Z. Zhang, G.-P. Jiang, A.H. Mamaghani, S. Sy, R. Gao, Y. Jiang, Y.-P. Deng, Z.-Y. Bai, L. Yang, A.-P. Yu, Z.-W. Chen, Three-dimensionally ordered mesoporous Co<sub>3</sub>O<sub>4</sub> decorated with mg as bifunctional oxygen electrocatalysts for high-performance zinc-air batteries, *Nano Energy* 100 (2022), 107425.
- [45] H.-C. Sun, C.-W. Tung, Y. Qiu, W. Zhang, Q. Wang, Z.-S. Li, J. Tang, H.-C. Chen, C.-D. Wang, H.-M. Chen, Atomic metal-support interaction enables reconstruction-free dual-site electrocatalyst, *J. Am. Chem. Soc.* 144 (2022) 1174–1186.
- [46] J. Jiang, R. Sun, X. Huang, H. Cong, J. Tang, W. Xu, M. Li, Y. Chen, Y. Wang, S. Han, H. Lin, CoS<sub>2</sub> quantum dots modified by ZIF-67 and anchored on reduced graphene oxide as an efficient catalyst for hydrogen evolution reaction, *Chem. Eng. J.* 430 (2022), 132634.
- [47] S. Liu, Y. Jiang, M. Yang, M. Zhang, Q. Guo, W. Shen, R. He, M. Li, Highly conductive and metallic cobalt-nickel selenide nanorods supported on Ni foam as an efficient electrocatalyst for alkaline water splitting, *Nanoscale* 11 (2019) 7959–7966.
- [48] M. Qu, Y. Jiang, M. Yang, S. Liu, Q. Guo, W. Shen, M. Li, R. He, Regulating electron density of NiFe-P nanosheets electrocatalysts by a trifle of Ru for high-efficient overall water splitting, *Appl. Catal. B: Environ.* 263 (2020), 118324.
- [49] X. Liu, J.-S. Meng, J.-X. Zhu, M. Huang, B. Wen, R.-T. Guo, L.-Q. Mai, Comprehensive understandings into complete reconstruction of precatalysts: synthesis, applications, and characterizations, *Adv. Mater.* 33 (2021), 2007344.
- [50] W. Zhang, N. Han, J. Luo, X. Han, S. Feng, W. Guo, S. Xie, Z. Zhou, P. Subramanian, K. Wan, J. Arbiol, C. Zhang, S. Liu, M. Xu, X. Zhang, J. Fransaer, Critical role of phosphorus in hollow structures cobalt-based phosphides as bifunctional catalysts for water splitting, *Small* 18 (2021), e2103561.
- [51] S. Ye, J. Wang, J. Hu, Z. Chen, L. Zheng, Y. Fu, Y. Lei, X. Ren, C. He, Q. Zhang, J. Liu, Electrochemical construction of low-crystalline CoOOH nanosheets with short-range ordered grains to improve oxygen evolution activity, *ACS Catal.* 11 (2021) 6104–6112.
- [52] X. Zhao, Q. Han, J. Li, X. Du, G. Liu, Y. Wang, L. Wu, Z. Chen, Ordered macroporous design of sacrificial Co/VN nano-heterojunction as bifunctional

- oxygen electrocatalyst for rechargeable zinc-air batteries, *Chem. Eng. J.* 433 (2022), 133509.
- [53] Q. Gao, W. Luo, X.-Y. Ma, Z.-M. Ma, S.-J. Li, F.-L. Gou, W. Shen, Y.-M. Jiang, R.-X. He, M. Li, Electronic modulation and vacancy engineering of  $\text{Ni}_9\text{S}_8$  to synergistically boost efficient water splitting: active vacancy-metal pairs, *Appl. Catal. B: Environ.* 310 (2022), 121356.
- [54] S. Wang, D. Yu, L. Dai, Polyelectrolyte functionalized carbon nanotubes as efficient metal-free electrocatalysts for oxygen reduction, *J. Am. Chem. Soc.* 133 (2011) 5182–5185.
- [55] J. He, W.-Q. Li, P. Xu, J.-M. Sun, Tuning electron correlations of  $\text{RuO}_2$  by co-doping of Mo and Ce for boosting electrocatalytic water oxidation in acidic media, *Appl. Catal. B: Environ.* 298 (2021), 120528.
- [56] R.-P. Li, Y.-Q. Li, P.-X. Yang, P.-H. Ren, D. Wang, X.-Y. Lu, R.-Y. Xu, Y.-H. Li, J.-M. Xue, J.-Q. Zhang, M.-Z. An, J.-Y. Ma, B. Wang, H.-K. Liu, S.-X. Dou, Synergistic interface engineering and structural optimization of non-noble metal telluride-nitride electrocatalysts for sustainably overall seawater electrolysis, *Appl. Catal. B: Environ.* 318 (2022), 121834.
- [57] A.-J. Medford, A. Vojvodic, J.-S. Hummelshøj, J. Voss, F. Abild-Pedersen, F. Studt, T. Bligaard, A. Nilsson, J.-K. Nørskov, From the Sabatier principle to a predictive theory of transition-metal heterogeneous catalysis, *J. Catal.* 328 (2015) 36–42.
- [58] S.-L. Hu, W.-X. Li, Sabatier principle of metal-support interaction for design of ultrastable metal nanocatalysts, *Science* 374 (2021) 1360–1365.